ACS Catalysis

Research Article

Cite This: ACS Catal. 2017, 7, 7431-7441

pubs.acs.org/acscatalysis

Catalysis at the Rim: A Mechanism for Low Temperature CO Oxidation over Pt_3Sn

Matthias Vandichel,* Alina Moscu, and Henrik Grönbeck*

Department of Physics and Competence Centre for Catalysis, Chalmers University of Technology, 412 96 Göteborg, Sweden

Supporting Information

ABSTRACT: Metal alloying is commonly used as a design strategy for catalyst optimization. The mechanistic understanding of this class of systems is, however, obscured by reaction induced segregation phenomena. Herein, the case of CO oxidation over Pt_3Sn is investigated using density functional theory calculations combined with ab initio thermodynamics and first-principles based microkinetic modeling. It is found that Pt_3Sn segregates under typical operating conditions into SnO_X and an Sn deficient metal phase. The segregation is driven both by the stability of the metal oxide and the strong bonding of CO to Pt. The catalytic consequences of a metal supported SnO_2 phase are explored by comparing CO oxidation at an SnO_X/Pt interface with oxidation over Pt and Pt/Pt_3Sn skin models. The reaction is found to proceed with lower barriers at the interface as compared to the metal-only systems and the cocatalytic role of the SnO_X rim is manifested by low temperature activity. The present work highlights the effects of reaction-induced metaloxide/metal interfaces and elucidates the role of Sn in PtSn alloys for CO oxidation reactions.

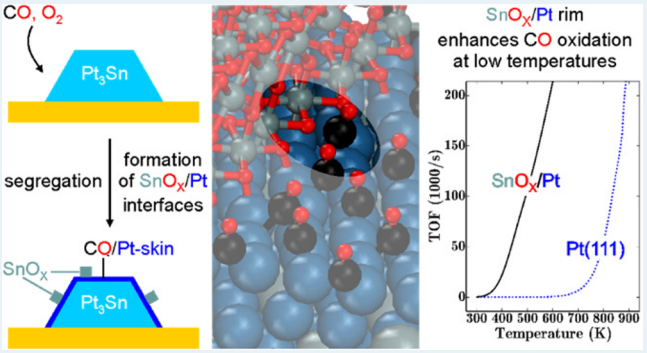

KEYWORDS: *bimetallic catalysts, CO oxidation, heterogeneous catalysts, metal oxide formation, ab initio microkinetic model*

INTRODUCTION

Heterogeneous catalysis is the main technology for chemical transformations and decisive for emission control and innovative sustainable energy systems.[1−4] The central role of heterogeneous catalysts in society motivates the considerable efforts invested to develop systems with high activity and selectivity. Supported metal nanoparticles represent a major fraction of heterogeneous catalysts, and one route to tailor the chemical properties of these systems is metal alloying. The mixing pattern in metal nanoalloys is generally complex and depends both on the constituent metals and the synthesis method. Various situations have been observed including core−shell structures, heterostructures, and mixed alloy nanoparticles.[5] The effects of alloying on catalytic properties are generally described in terms of ensemble, ligand, and strain effects.[6−9] Ensemble effects refer to geometric adsorption constraints upon alloying, whereas ligand and strain effects denote changes in the electronic structure.

Platinum is a precious metal commonly used for catalytic oxidation reactions. Pt alloying with less noble metals has in the past shown to enhance the activity for numerous reactions. One example is the oxygen reduction reaction in the proton-exchange membrane fuel cell (PEM-FC) in which alloying with lanthanides[9,10] has shown to enhance the activity considerably. In this case, the beneficial alloy effect originates from strain effects as a compressed Pt overlayer is formed on the surface of the bulk. Another example is preferential CO oxidation in the presence of H_2 (PROX) which is used to purify an H_2 stream from trace amounts of CO. This is an important process within, for example, PEM-FC technology as small amounts of CO poison the electrode catalysts. An ideal PROX-catalyst should selectively promote the CO oxidation without catalyzing the parallel oxidation of hydrogen to water. Different Pt alloys, such as PtCo, PtFe, and PtSn, have shown promise as efficient PROX catalysts.[11−14] Furthermore, Pt-group metals supported on ceria which have been measured to have a selectivity for CO oxidation reaching nearly hundred percent for Pt/CeO_2 at low temperatures.[15] A prerequisite for efficient PROX is a low temperature activity for CO oxidation. Such low temperature activity has been observed for promoted Pt-group metals[16] and in the case of FeO_x/Pt(111), the activity was rationalized by the possibility to have CO oxidation at a FeO_x/Pt interface.[17] In general, however, the mechanistic origin of the favorable CO oxidation for bimetallic alloys has been difficult to disentangle. In the case of Pt_3Sn, the CO oxidation activity at low temperature has been related to facile CO oxidation over the alloy surface.[18] In particular, CO oxidation in the high coverage regime was found to proceed with lower barriers on Pt_3Sn(111) than on the pristine Pt(111) surface.[18,19] The promoting effect of Sn was in this case attributed to electronic ligand effects.

Received: June 26, 2017
Revised: August 27, 2017
Published: September 12, 2017

DOI: 10.1021/acscatal.7b02094
ACS Catal. 2017, 7, 7431−7441

The dynamic response of metal nanoparticles to adsorbates makes it challenging to assess the origin of promoting effects upon alloying. Several studies have demonstrated that reactions may drive surface reconstruction and segregation.[20,21] Also in the case of PtSn nanoparticles, experimental evidence exists for adsorbate induced segregation during typical operating conditions for regular CO-oxidation.[22] In ref 22, ambient pressure X-ray photoelectron spectroscopy (XPS) showed the formation of a Sn oxide phase during CO-oxidation over silica supported PtSn nanoparticles. Based on the experiments,[22] it was suggested that CO oxidation occurs with a low activation barrier at the interface between Pt and SnO_X domains in a Mars–van Krevelen mechanism.[23] Moreover, a SnO_2 phase in contact with PtSn nanoalloys was observed with transmission electron microscopy analysis of a PtSn catalyst for CO electro-oxidation.[24] The existence of Pt–Sn segregation during CO exposure over alumina supported PtSn has furthermore been inferred from *in situ* diffuse reflectance IR Fourier transform spectroscopy (DRIFTS) following the CO stretch vibration.[11,12,25] Segregation and subsequent tin-oxide formation has also been observed with XPS for $Pt_3Sn(111)$ single crystal surfaces exposed during CO oxidation.[26] At elevated pressures of CO and O_2 it was proposed that $Pt_3Sn(111)$ converts to an inverse catalyst with SnO_X supported by metallic Pt_3Sn.[26]

Given the growing experimental evidence for segregation of PtSn nanoparticles and $Pt_3Sn(111)$ surfaces, it becomes warranted to understand the stability of these inverse (SnO_X/Pt) catalysts together with their activity for CO oxidation. Herein, CO oxidation over $Pt_3Sn(111)$ is investigated using density functional theory calculations combined with *ab initio* thermodynamics and microkinetic modeling. Our results demonstrate the preference for segregation during typical reaction conditions with the formation of an SnO_X phase. Furthermore, the cocatalytic effect of an metaloxide/metal interface is elucidated by comparing the reaction kinetics over SnO_X/Pt with pristine Pt(111) and Pt(111) supported on Pt_3Sn.

THEORETICAL METHODOLOGY

Density functional theory (DFT) is applied with the gradient corrected exchange-correlation functional according to Perdew, Burke, and Ernzerhof (PBE).[27] In particular, the Vienna Ab Initio Simulation Package (VASP)[28,29] is used. The one-electron Kohn–Sham orbitals are expanded in a plane-wave basis-set with a kinetic energy cutoff of 450 eV. PAW potentials are employed to describe the interaction between the valence electrons and the core.[30] Reciprocal space integration over the Brillouin zone is approximated with finite sampling using Monkhorst–Pack grids.[31,32] Bulk calculations of Pt, Sn, Pt_3Sn, SnO, and SnO_2 use a *k*-point grid of at least 12 × 12 × 12. Surface calculations are performed using five layered orthorhombic slabs; $(4 \times 2\sqrt{3})$rect for metal surfaces and $(6 \times 2\sqrt{3})$rect for metal-supported SnO_2 using *k*-point grids of 3 × 3 × 1 and 2 × 3 × 1, respectively. The systems are structurally optimized until the largest force is smaller than 0.03 eV/Å. Transition states are obtained initially with the climbing image nudged elastic band[33,34] and further refined with the dimer method.[35] The convergence criteria for the transition state searches are set to at least 0.05 eV/Å. To verify transition states and local minima, a relevant partial Hessian vibrational analysis (PHVA) is employed. The PHVA is performed only for the surface species while keeping the rest of the system fixed. The PHVA is used also to obtain zero-point corrections and free energy contributions.[36,37] The numerical partial Hessian is calculated by displacements in *x*, *y*, and *z*-directions of ±0.02 Å, and the vibrational modes are extracted using the normal-mode analysis as implemented in the postprocessing toolkit TAMKIN.[38]

The bulk structures of Pt, Sn, Pt_3Sn, SnO, and SnO_2 are optimized to obtain the cell parameters.[39] The lattice parameters are overestimated by 1–2% with respect to experiments and in good agreement with previous studies using the same xc-functional (see Table 1 in the Supporting Information). The analysis of the bulk systems provides the relative stabilities of the different phases. For example, the alloy formation energy of Pt_3Sn from bulk Pt and bulk Sn is found to be exothermic by −1.53 eV per Pt_3Sn unit. This is in line with experimental observations, showing that PtSn is stable under inert conditions.[24] The oxidation of Pt_3Sn is exothermic with reaction energies of −1.13 and −3.51 eV for formation of monometallic Pt and SnO and SnO_2, respectively (Table 2). *Ab initio* thermodynamics[40,41] is used to evaluate the relative stabilities of different segregation possibilities of $Pt_3Sn(111)$ as a function of CO and oxygen chemical potential. In this way, the thermodynamic preference between the considered systems can be evaluated as a function of temperature and pressure.[40,42] The initial configuration in the analysis is a bare $Pt_3Sn(111)$ surface together with CO and O_2 in the gas phase. The change in surface energy ($\Delta\gamma_0$) is calculated as a function of the gas phase chemical potentials of CO (μ_{CO}) and O_2 (μ_O):

$$\Delta\gamma_0(T, p, N_{Pt_3Sn}, N_O, N_{CO}) = \frac{1}{A}(E^{slab}_{Pt_3Sn}(T, p, N_O, N_{CO}) - E^{slab}_{Pt_3Sn}(T, p, N_O = 0, N_{CO} = 0) - N_O\mu_O(T, p) - N_{CO}\mu_{CO}(T, p)) \quad (1)$$

Here, $E^{slab}_{Pt_3Sn}$ represents the electronic energy of the surface with N_O surface oxygen atoms and N_{CO} carbon mono-oxide molecules, and *A* is the area of the surface cell. Upon segregation, it is reasonable to assume that the exposed Sn surface atoms will form a SnO_X phase. In the first instance, this can be approximated with the formation of a bulk SnO_2 phase together with a Pt-overlayer (Pt-skin) supported by the Pt_3Sn alloy. Here, such a system is denoted by $Pt(111)/Pt_3Sn$. To model this process, the Pt atoms replacing the Sn atoms in the surface are taken from a Pt_3Sn-bulk reservoir. To correct for an additional Sn atom per three Pt atoms, we assume that extra SnO_2 is formed. The process is graphically represented in the Supporting Information (Figure S1). The relationship describing the change in stability relative to the bare Pt_3Sn surface slab is given by

$$\Delta\gamma_i(T, p, N_{SnO_2}, N_{Pt_3Sn}, N_O, N_{CO}) = \frac{1}{A}\left(E^{slab}_{Pt/Pt_3Sn}(T, p, N_{SnO_2}, N_O, N_{CO}) + \left(\frac{4}{3}\right)N_{SnO_2}E^{bulk}_{SnO_2} - \left(\frac{1}{3}\right)N_{SnO_2}E^{bulk}_{Pt_3Sn} - E^{slab}_{Pt_3Sn}(T, p, N_O = 0, N_{CO} = 0) - \left(N_O + \left(\frac{8}{3}\right)N_{SnO_2}\right)\mu_O(T, p) - N_{CO}\mu_{CO}(T, p)\right) \quad (2)$$

DOI: 10.1021/acscatal.7b02094
ACS Catal. 2017, 7, 7431–7441

Table 1. CO and Oxygen Adsorption Energies Evaluated in $(4 \times 2\sqrt{3})$rect Surface Cells at Different Coverages for Pt(111), $Pt_3Sn(111)$, and $Pt(111)/Pt_3Sn$[a]

	coverage (ML)	$E_{ads,CO}$	$E_{ads,O}$	$\Delta E^{\ddagger}$
Pt(111)	**0.0625**	−1.91 (hcp)	−1.27 (fcc)	1.00
Pt(111)	**0.25**	−1.80 (hcp)	−1.25 (fcc)	
Pt(111)	**0.5**	−1.69 (b)	−0.92 (4 fcc and 4 b)	
$Pt_3Sn(111)$	**0.0625**	−1.94 (Pt_3-hcp)	−1.28 (Pt_2Sn-fcc)	1.07
$Pt_3Sn(111)$	**0.25**	−1.65 (Pt_3-hcp)	−1.14 (Pt_2Sn-fcc)	
$Pt_3Sn(111)$	**0.5**	−1.33 (Pt-t)	−1.12 (Pt_2Sn-fcc)	
$Pt(111)/Pt_3Sn$	**0.0625**	−2.09 (fcc-Pt)	−1.36 (fcc-Pt)	1.11
$Pt(111)/Pt_3Sn$	**0.25**	−1.92 (fcc-Pt)	−1.40 (fcc-Pt)	
$Pt(111)/Pt_3Sn$	**0.5**	−1.74 (b)	−1.11 (fcc-Pt)	

[a]The adsorption energies are calculated with respect to gas phase CO and O_2. The adsorption site is indicated [fcc-hollow (fcc), hcp-hollow (hcp), bridge (b), and atop (t)]. Pt_3-hcp and Pt_2Sn-fcc denote hollow positions composed of three and two Pt atoms, respectively; fcc-Pt denotes an fcc position with Pt in the third atomic layer. In the case of $Pt_3Sn(111)$ with 0.5 ML O, a pronounced structural relaxation occurred, where one of the four Sn atoms relaxed out of the surface. Energies are reported in electronvolts.

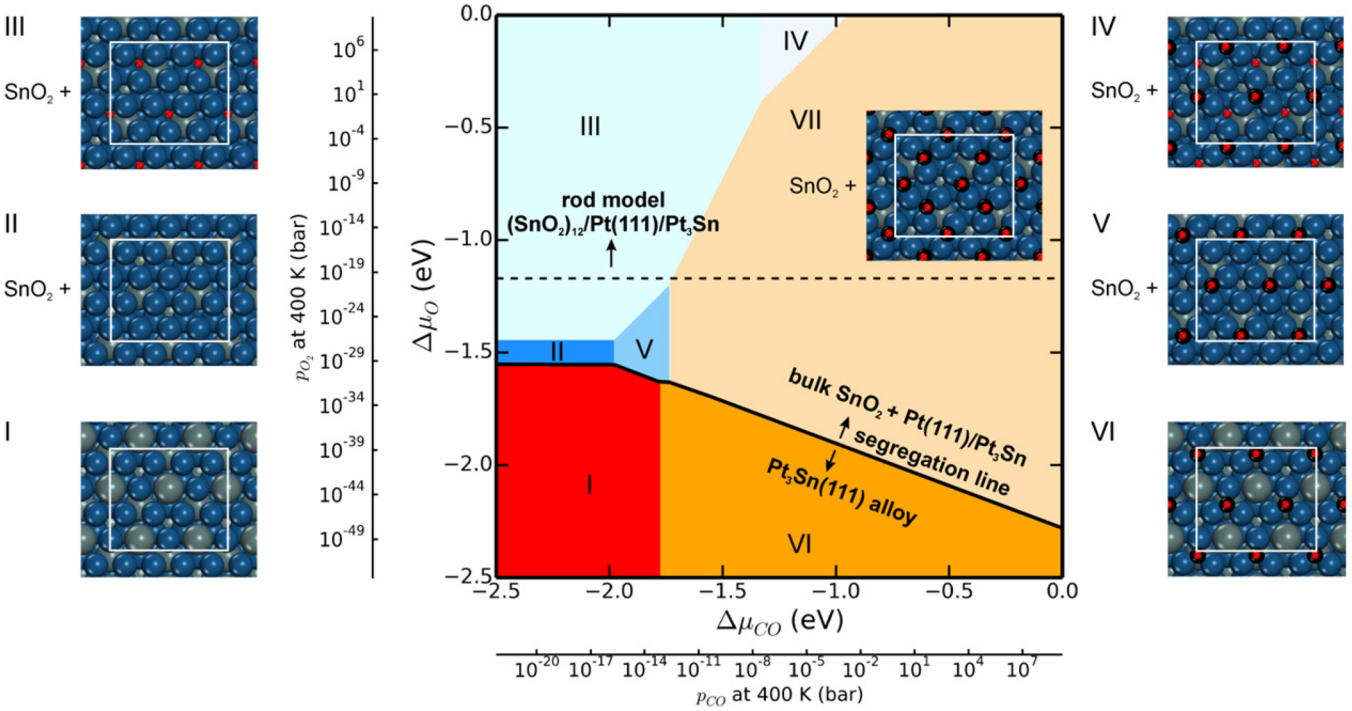

Figure 1. Thermodynamic phase diagram showing the preferred phase (lowest $\Delta\gamma$ in eq 2) as a function of differences in chemical potential ($\Delta\mu_i$) for CO and O_2. The solid black line indicates segregation from a $Pt_3Sn(111)$ surface to $Pt/Pt_3Sn(111)$ and bulk SnO_2. Structural models for phases **I–VII** are shown. The dotted line shows the conditions when the formation of the rod model in Figure 2a and b becomes thermodynamically preferred. The surface cells are indicated by white rectangles. Atomic color codes: C in black, O in red, Sn in green, and Pt in blue.

Here, E^{slab}_{Pt/Pt_3Sn}, $E^{bulk}_{SnO_2}$, and $E^{bulk}_{Pt_3Sn}$ denote the electronic energy of the Pt-skin system, SnO_2 bulk, and Pt_3Sn bulk, respectively. The vibrational and entropy contributions to bulk and surfaces energies are neglected in this analysis. In the absence of segregation ($N_{SnO_2} = 0$), this expression simplifies to eq 1. We refer the reader to the Supporting Information for details on the expansion of the chemical potentials to partial pressures p_{CO} and p_{O_2}.

RESULTS AND DISCUSSION

We present first a thermodynamic analysis of $Pt_3Sn(111)$ and thereafter results related to CO oxidation. The thermodynamic analysis provides means to establish the relevant catalyst phases during reaction conditions. On the basis of the analysis, structural models are constructed and evaluated with respect to CO oxidation by calculations of reaction barriers and a microkinetic analysis.

A. Thermodynamic Analysis. In the following section, the adsorption energies of atomic oxygen (O) and carbon monoxide (CO) on surface models of Pt(111), $Pt_3Sn(111)$, and $Pt(111)/Pt_3Sn$ are discussed. Representative structures are, thereafter, presented in a phase diagram to investigate segregation possibilities.

CO and O Adsorption on Pt(111), $Pt_3Sn(111)$, and $Pt(111)/Pt_3Sn$. Adsorption of CO and oxygen is investigated on Pt(111), $Pt_3Sn(111)$, and $Pt(111)/Pt_3Sn$ and the results are reported in Table 1. The adsorption properties are calculated at three different coverages. The coverage dependence is similar for CO and oxygen (O) in the sense that the adsorption

DOI: 10.1021/acscatal.7b02094
ACS Catal. 2017, 7, 7431−7441

energies decrease with coverage. The strongest coverage dependence is predicted for CO on $Pt_3Sn(111)$, whereas O has a low coverage dependence on this surface. The barrier for CO and O association to CO_2 is calculated in the low coverage regime (1/16 ML in each of the adsorbates) with respect to CO and oxygen in separate surface cells. The barrier on Pt(111) is calculated to be 1.00 eV which is in good agreement with previous results.[43] The reaction proceeds by diffusion of CO to an atop site and the bond forms over the fcc site where oxygen initially is bonded. The mechanism is similar on the other two surfaces. The barrier is slightly higher on the $Pt_3Sn(111)$ and $Pt(111)/Pt_3Sn$ which in the case of $Pt_3Sn(111)$ is related to a stronger bonded CO whereas for $Pt(111)/Pt_3Sn$ it originates from a strong oxygen bond. CO oxidation over Pt(111) and $Pt_3Sn(111)$ has previously been compared computationally by Dupont et al.[18] using a similar computational approach as the present one. With a coverage of 0.25 ML in each adsorbate, barriers of 0.82 and 0.68 eV were reported for Pt(111) and $Pt_3Sn(111)$, respectively. The barriers were in this case[18] calculated with respect to coadsorbed CO and O in the same surface cell. Relating those barriers instead to CO and O in separate surface cells, barriers of 1.06 [Pt(111)] and 0.93 eV [$Pt_3Sn(111)$] are obtained. Comparing our results in Table 1 with the results in ref 18 demonstrates pronounced coverage dependences on the reaction barriers that are different for Pt(111) and $Pt_3Sn(111)$. The result shows that barriers evaluated at high coverage are not necessarily representative for the low coverage regime. Comparing CO oxidation over Pt(111) and $Pt_3Sn(111)$, the differences in coverage dependences lead to opposite conclusions regarding the reaction rate on the two surfaces. The barrier calculated at high coverage suggests that the reaction is faster on $Pt_3Sn(111)$ than Pt(111), whereas the barrier evaluated in the low coverage regime suggest the opposite. As the experimental CO:O coverage ratio rarely equals 1, it is preferable to evaluate the barrier at low coverage and subsequently add coverage dependences for CO and oxygen.

Phase Diagram for Pt_3Sn in the Presence of CO and O. Knowing the adsorption energies of CO and oxygen on Pt(111) and $Pt_3Sn(111)$, it becomes important to study possible phase segregation scenarios. As the adsorption energies at high CO coverage (0.5 ML) are stronger on Pt(111) as compared to $Pt_3Sn(111)$, it is reasonable to assume surface reordering where bare platinum is exposed to the gas-phase and an SnO_2 phase is formed.[44] To study this hypothesis, we construct a phase diagram, see Figure 1. Eight different phases are considered in the diagram, namely (**I**) the bare $Pt_3Sn(111)$ surface, (**II**) a segregated system with a Pt-skin supported on $Pt_3Sn(111)$ together with SnO_2 in the bulk, (**III**) the segregated surface with 0.25 ML of O, (**IV**) the segregated surface with 0.25 ML of O and 0.25 ML CO, (**V**) the segregated surface with 0.25 ML CO, (**VI**) the $Pt_3Sn(111)$ surface with 0.25 ML CO, (**VII**) the $Pt_3Sn(111)$ surface with 0.5 ML CO, and (**VIII**) the $Pt_3Sn(111)$ surface with 0.25 ML O. Only seven of the phases appear in the phase diagram as the adsorption energy of oxygen on the alloy surface is too low at 0.25 ML to make this phase (**VIII**) present. The phase diagram is an approximation, in the sense that in reality a metal supported SnO_2 phase would form instead of a bulk SnO_2 phase.[45] A general limitation of an *ab initio* thermodynamics analysis is, of course, that only considered phases are ranked whereas other possible structural configurations are not considered.

The $Pt_3Sn(111)$ surface is preferred at low chemical potentials of CO and oxygen. Increasing only the oxygen chemical potential predicts segregation with the formation of the Pt-skin system [$Pt(111)/Pt_3Sn$] and bulk SnO_2. Further increase of the oxygen chemical potential results in adsorbed oxygen on $Pt(111)/Pt_3Sn$. Increasing the CO chemical potential while keeping the oxygen chemical low preserves the alloy and results in CO adsorbed on $Pt_3Sn(111)$. A combined CO and oxygen environment from this point will again promote segregation (moving from **VI** to **VII**). It is interesting that the presence of CO on the alloy surface lowers the required oxygen pressure for segregation. The segregation line has a negative slope for changes in the CO chemical potential starting at around −1.75. CO oxidation is typically studied around 400 K and CO and oxygen partial pressures of 1.1×10^{-2} and 2.14×10^{-2} bar, respectively. During these conditions, our analysis reveals that the alloy is preferably segregated. This corresponds to phase **VII**, being the Pt-skin system covered with CO. A phase with mixed CO/O coverage, here modeled with 0.25 ML of CO and 0.25 ML of oxygen (**IV**), appears only at higher oxygen pressures and reduced CO pressures.

The prediction that Pt_3Sn will segregate to a surface rich in Pt and SnO_2 (SnO) is consistent with experiments.[22] *In situ* diffuse reflectance IR Fourier transform spectroscopy (DRIFTS) measurements on PtSn exposed to CO have shown a shift in the CO stretch vibration while ramping down the temperature from 175 to 50 °C.[12] The CO vibrational peak shifted from 2054 cm^{-1} at 175 °C to 2071 cm^{-1} at 50 °C which is close to the value for CO adsorbed on Pt (2077 cm^{-1}).[25] Decreasing the temperature at constant CO pressure results in an increased chemical potential which drives the segregation as shown in the phase diagram. The formation of an SnO_2 phase is, furthermore, in accordance with XPS measurements.[22,25,26] Phase diagrams at different temperatures are given in the Supporting Information.

B. CO Oxidation at the SnO_X/Pt Interface. *Atomistic Model.* From the phase diagram (Figure 1) and previous experiments,[22] it is clear that SnO_X/Pt interfaces will be present during CO oxidation. After segregation, we envision a scenario in which SnO_2−islands are formed on a Pt-skin system. We represent this situation computationally with a two-layer SnO_2-rod supported on a Pt-skin (Figure 2a and b). The rod exposes (110) surfaces to the gas-phase and the metal surface as this surface is the stable surface of SnO_2. The lattice of the SnO_2 is expanded by 2% in the direction of the rod to fit the Pt_3Sn lattice. The rod was placed at different positions on the metal surface and the lowest energy configuration was chosen for further investigations. Because of the finite dimension of the rod, a somewhat higher oxygen chemical potential (−1.17 eV) is required for segregation than in the case of SnO_2 bulk formation. However, the thermodynamic analysis shows that segregation to the rod is preferred at any relevant oxygen pressures; see Figure 1.

A range of different sites are present at the SnO_2/Pt-skin interface. The studied SnO_2 rod has three different oxygen atoms that potentially can react with CO. Note that the three oxygen atoms have different chemical environments. The reaction of CO with the three oxygen atoms generates a network of reactions that contains eight different states of the rod; see Scheme 1. We denote the three different oxygen atoms by A, B, and C and an oxygen vacancy by *. The corresponding adsorption energies and activation barriers are reported in

DOI: 10.1021/acscatal.7b02094
ACS Catal. 2017, 7, 7431−7441

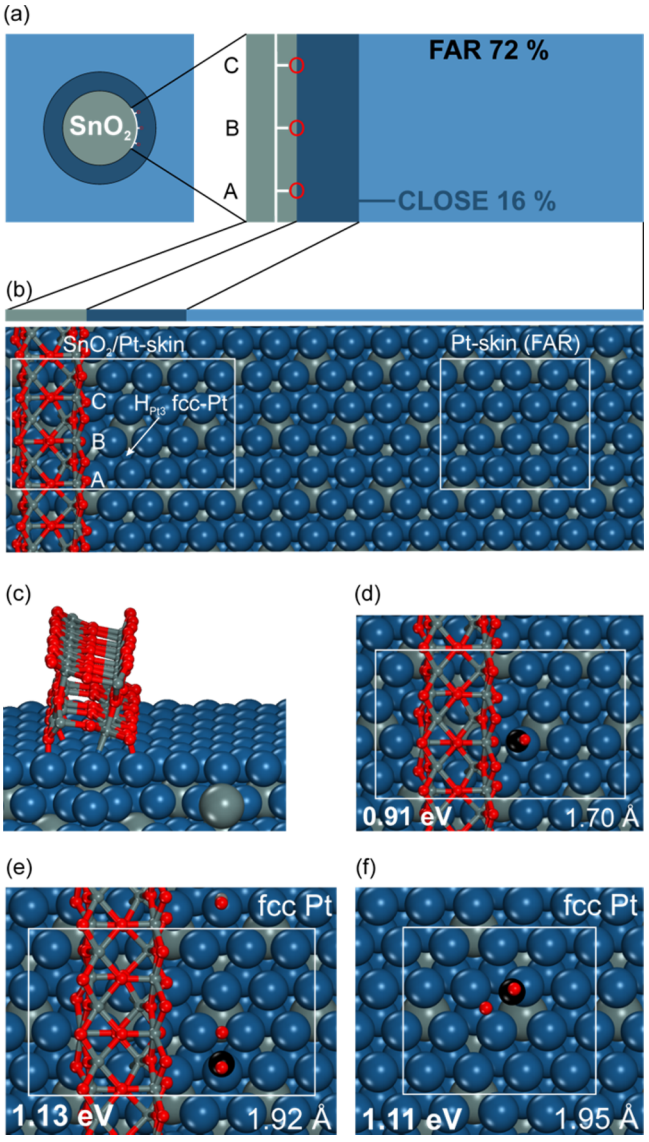

Figure 2. (a) Site distribution used in the mean field microkinetic model (12% SnO_X, 16% CLOSE and 72% FAR) with three different oxygen states within the SnO_2 states (A, B, C). (b) Surface cells with rod $(6 \times 2\sqrt{3})$rect and without rod $(4 \times 2\sqrt{3})$rect, (c) side view of rod system, (d–f) overview of included CO oxidation transition states (TS), with O–CO distance in TS (Å) and activation barrier (eV) relative to O and CO in separate unit cells. Reaction at the rod (ABC → A*C) (d) On the Pt-skin surface, the TS occurs preferably over fcc Pt sites. Barriers on fcc Pt sites for CLOSE (e) and FAR (f) sites are very similar.

Table 2. CO adsorbs in an fcc-Pt site close to the rod with a slightly lower adsorption energy (about −1.99 eV) than on the skin system without the rod at a coverage of 0.0625 ML. The vacancy formation energies of the oxygen atoms in the rod are sensitive to the state of the rod. Removal of the central oxygen (B) forming 1/2 O_2 in the gas-phase is endothermic by 1.24 eV (ABC → A*C). Subsequent removal of oxygen atom A is endothermic by 1.04 eV (A*C → A**). Going instead from A*C to **C by removal of oxygen atom C requires an energy of 1.26 eV. The lowest depletion energy in the network is (*B* → ***) being 0.90 eV and the highest depletion energy is 1.53 eV for (AB* → *B*).

CO oxidation is one possibility to deplete oxygen atoms from the (SnO_2)-rod and create oxygen vacancies. The activation barriers for CO oxidation at the SnO_2/metal interface are strongly dependent on the state of the rod. The barriers are evaluated with respect to CO in the fcc-Pt position close to position B, and thus represent an upper bound of the barrier. The lowest barrier is calculated for (ABC → A*C) being 0.91 eV. CO oxidation from the B site results in a low barrier also in the case of a reduced rod. This is, for example, seen for the (AB* → A**) transition which has a barrier of 0.99 eV. The barriers at the interface are considerably lower than the barrier for CO oxidation on the Pt-skin which is 1.11 eV. The low barrier at the interface is likely connected to a favorable transition state geometry. The CO−O distance is only 1.70 Å at the transition state which should be compared to 1.95 Å on the Pt-skin. The barriers for further reaction with oxygen atoms from A*C are 1.10 eV (A*C → **C) and 1.20 eV (A*C → A**), respectively. Besides the CO oxidation barrier for (ABC → A*C), also the barrier for (AB* → A**) is low, being 0.99 eV. Higher barriers (>1.22 eV) were obtained for the CO oxidations (ABC → AB*, 1.26 eV), (ABC → *BC, 1.22 eV), (AB* → *B*, 1.29 eV), and (*BC → *B*, 1.33 eV). We have also considered the possibility to adsorb molecular oxygen at the B-site (A*C). The adsorption energy is −0.51 eV. With molecular oxygen at the B-position of the rod, we could have included this state into Scheme 1 as a state prior ABC (A–BO–C). However, the barrier for direct CO oxidation from this state is 1.52 eV. Thus, this path will not contribute to the catalytic activity at low temperatures and was not included in the microkinetic modeling. For structures of the reactant, transition state and product state for CO oxidation from A–BO–C → ABC; see the Supporting Information.

The different states of the rod in Scheme 1 are connected either through CO oxidation, oxygen transfer, or reoxidation by O_2 from the gas phase. The barriers for oxygen transfer are between 0.74 and 1.41 eV (Table 3). The barriers for reoxidation with molecular oxygen are found to be below 0.8 eV, which makes these processes fast with respect to CO oxidation. The adsorption and reaction energies together with the relative stabilities of the different states of the rod suggest feasible catalytic cycles, for example ABC→ A*C → **C → ABC. This path together with other possibilities has been evaluated by construction of a mean field microkinetic model.

Construction of a Kinetic Model. To evaluate the catalytic behavior of the SnO_2/metal interface, a first-principles based microkinetic model (MKM) is constructed. The model considers sites for CO oxidation at the SnO_2/metal interface (CLOSE) as well as the regular Pt-skin metal (FAR). To find an appropriate distribution between CLOSE, FAR, and sites blocked by the SnO_2 phase in the MKM, we consider a typical Pt_3Sn nanoparticle of 4 nm. The total exposed surface area of such a hemispherical nanoparticle is 25 nm^2. Upon segregation, a Pt-skin system is formed with a SnO_2 deposit. We assume that 12% percent of the Pt-skin sites are blocked by the SnO_2-phase having a spherical shape with a diameter of 2 nm. The CLOSE sites are defined as sites within 0.5 nm from the perimeter of the SnO_2 deposit, thus 16% of the total number of sites. Regular Pt-skin sites constitute the FAR sites and amount to 72% of the total number of sites. Two atomistic models are considered to describe the reactions (Figure 2b). Adsorption on SnO_2-sites and SnO_2/Pt-skin interface sites are investigated with a periodic rod. This system is described in detail in the Theoretical Methodology section and the Supporting Informa-

DOI: 10.1021/acscatal.7b02094
ACS Catal. 2017, 7, 7431−7441

Scheme 1. Considered Reactions for the SnO_X/Metal Interface within the Mean-Field Microkinetic Model[a]

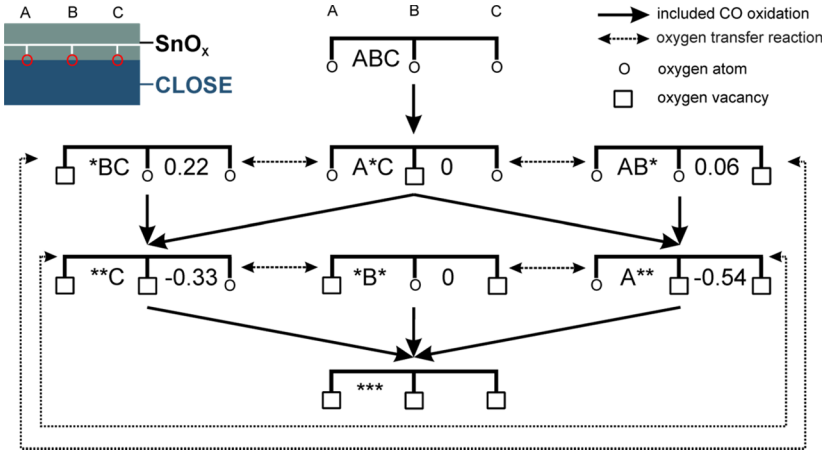

[a]The energy differences between SnO_X states with the same number of oxygen atoms are given in electronvolts.

Table 2. CO Adsorption Energies [E_{ads}(CO)], Oxygen Vacancy Formation Energies [E_{vac}(O)], and Reaction Barriers ($\Delta E^{\ddagger}$) on Pt(111)/Pt_3Sn[a]

	E_{ads}(CO)	site O	E_{vac}(O)	$\Delta E^{\ddagger}$
ABC → A*C	−1.99	ABC	−1.24	0.91
A*C → A**	−1.99	A*C	−1.04	1.20
A*C → **C	−1.99	A*C	−1.26	1.10
AB* → A**	−1.99	AB*	−0.99	0.99
***BC → **C**	−1.99	*BC	−1.03	1.03
****C → *****	−1.90	**C	−1.23	1.12
B* → **	−2.00	*B*	−0.90	1.13
A → *****	−1.98	A**	−1.45	1.09

[a]E_{ads} for CO is calculated with the molecule adsorbed in an fcc-Pt position in front of the rod; see Figure 2b. The positions for the oxygen atoms in the rod are labeled according to Scheme 1. The energies are reported without zero-point corrections in electronvolts.

tion. The SnO_2/Pt interface sites are modeled with a $(6 \times 2\sqrt{3})$rect surface cell, while the regular Pt-skin sites are modeled with a $(4 \times 2\sqrt{3})$rect surface cell.

The overall reaction is described by a set of coupled differential equations with O and CO coverages for the different areas:

$$\frac{\partial \theta_i(t)}{\partial t} = \sum_j c_{ij} r_j(\theta_1(t), ..., \theta_N(t)) \quad (4)$$

$\theta_i(t)$ represents the coverage of adsorbate i at time t. c_{ij} are the stoichiometric numbers, and r_j the elementary reaction rates. (All implemented differential equations are given explicitly in the Supporting Information.) To obtain steady-state coverages and turnover frequencies, this set of coupled differential equations is integrated numerically using the SciPy[46] Python package with the VODE solver for stiff problems.

In total 23 reaction steps are considered in the model including O_2 adsorption and desorption, CO adsorption and desorption, CO oxidation at CLOSE and FAR sites, oxygen transfer reactions and reoxidation of the SnO_X phase by O_2. All reaction steps are given in Table 3. To obtain numerical stability, the CO and O adsorption energies at the CLOSE sites are approximated with the values for the FAR sites. The entropic differences for adsorption and desorption processes are calculated by considering immobile adsorbed species for which the entropy is calculated within the harmonic approximation. The known difference in sticking coefficients of CO and O_2 on Pt(111)[47] is accounted for by applying sticking coefficients of 0.9 and 0.1 for CO and O_2, respectively. To describe the overall reaction kinetics, it is crucial to consider adsorbate−adsorbate interactions. The repulsive CO−CO, CO−O, O−CO, and O−O coverage dependences are obtained by a spline fitting procedure; see the Supporting Information for details. The dependencies for CO and O are fitted from calculations of differential adsorption energies at coverages ranging from 0.0625 to about 0.8 ML. The cross term for how CO (O) is affected by O (CO) is calculated in the limit of low CO (O) coverage, being 0.0625 ML. The adsorbate−adsorbate interactions were based on results for Pt(111). In the MKM, the CO oxidation barriers are linearly scaled with the CO coverage based on a fit of transition states barriers at different coverages (see the Supporting Information). To validate the kinetic model on Pt(111), we compare the light-off behavior with surface science experiments of CO-oxidation.[48] Light-off curves are simulated for Pt(111) at global pressures of 1 and 0.1 mbar and CO:O_2 pressure ratios of 2:1, 1:1, and 1:4 and our simulated light-off temperatures are within ±50 K of the experiments. Furthermore, the simulated turnover frequencies (TOFs) are in the same order of magnitude as reported experiments.[48] To account for the rapid diffusion of CO between FAR and CLOSE sites, a scrambling procedure was implemented which averages the CO coverages. The new coverages are calculated from the old coverages according to

$$\theta^{new}_{CO,CLOSE} = \left(\theta^{old}_{CO,CLOSE} + \theta^{old}_{CO,FAR}\frac{A_{close}}{A_{far}}SF_{CO}\right)\frac{1}{(1 + SF_{CO})}$$

$$\theta^{new}_{CO,FAR} = \theta^{old}_{CO,CLOSE}\frac{SF_{CO}}{(1 + SF_{CO})} + \theta^{old}_{CO,FAR}\left(1 - \frac{SF_{CO}}{(1 + SF_{CO})}\frac{A_{close}}{A_{far}}\right)$$

Here, the applied scrambling factor SF_{CO} was chosen to be 50%. The scrambling procedure was chosen instead of explicit diffusion steps due to numerical instabilities for a preliminary model including diffusion steps.

DOI: 10.1021/acscatal.7b02094
ACS Catal. 2017, 7, 7431−7441

Table 3. Considered Reaction Steps in the MKM[a]

no.	eq	K (−)	ΔG_r	ΔH_r	$-T\Delta S_r$	ΔE_r	ads site
Adsorption/Desorption Steps							
1	$CO(g) + *metal \leftrightarrow CO^{*metal}$	5.60×10^{06}	−0.78	−2.02	1.24	−2.09	fcc Pt
2	$O_2(g) + 2*metal \leftrightarrow 2O^{*metal}$	5.17×10^{10}	−1.33	−2.67	1.34	−2.72	fcc Pt
3	$O_2(g) + A^{**} \leftrightarrow ABC$	1.11×10^{07}	−0.86	−2.22	1.36	−2.28	A** (A and B)
4	$O_2(g) + **C \leftrightarrow ABC$	5.73×10^{08}	−1.08	−2.44	1.36	−2.49	**C (B and C)
5	$O_2(g) + *B^* \leftrightarrow ABC$	2.29×10^{11}	−1.41	−2.76	1.35	−2.82	*B* (A and C)
6	$O_2(g) + *** \leftrightarrow A^*C$	6.22×10^{08}	−1.08	−2.43	1.35	−2.48	*** (A and C)
7	$O_2(g) + *** \leftrightarrow AB^*$	1.32×10^{08}	−1.00	−2.37	1.37	−2.43	*** (B and C)
8	$O_2(g) + *** \leftrightarrow *BC$	6.40×10^{06}	−0.83	−2.20	1.38	−2.26	*** (A and B)
no.	eq		$\Delta E_f^{\ddagger}$	$\Delta H_f^{\ddagger}$	$-T\Delta S_f^{\ddagger}$	$\Delta E_b^{\ddagger}$	$\Delta H_b^{\ddagger}$	$-T\Delta S_b^{\ddagger}$
CO-Oxidation Steps								
9	$CO^{*metal} + O^{*metal} \leftrightarrow CO_2(g) + 2*metal$		1.11	1.07	0.06	0.91	0.88	2.09
10	$CO^{*metal} - ABC \leftrightarrow A^*C + CO_2(g) + *metal$		0.91	0.87	0.03	0.94	0.91	2.10
11	$CO^{*metal} - A^*C \leftrightarrow A^{**} + CO_2(g) + *metal$		1.20	1.16	0.03	1.42	1.39	2.06
12	$CO^{*metal} - A^*C \leftrightarrow **C + CO_2(g) + *metal$		1.11	1.07	0.02	1.11	1.08	2.04
13	$CO^{*metal} - A^{**} \leftrightarrow *** + CO_2(g) + *metal$		1.09	1.04	0.02	0.93	0.89	2.07
14	$CO^{*metal} - **C \leftrightarrow *** + CO_2(g) + *metal$		1.12	1.07	0.05	1.24	1.21	2.10
15	$CO^{*metal} - AB \leftrightarrow A^{**} + CO_2(g) + *metal$		0.99	0.94	0.07	1.26	1.23	2.13
16	$CO^{*metal} - *BC \leftrightarrow **C + CO_2(g) + *metal$		1.03	0.98	0.06	1.27	1.24	2.12
17	$CO^{*metal} - *B^* \leftrightarrow *** + CO_2(g) + *metal$		1.13	1.08	0.06	1.48	1.45	2.13
Oxygen Transfer Steps within the SnO_X-rod								
18	$A^*C \leftrightarrow AB^*$		0.79	0.74	0.09	0.74	0.68	0.06
19	$A^*C \leftrightarrow *BC$		1.03	0.97	0.09	0.81	0.75	0.06
20	$AB^* \leftrightarrow *BC$		1.29	1.23	0.06	1.13	1.07	0.05
21	$*B^* \leftrightarrow A^{**}$		0.87	0.81	0.06	1.41	1.35	0.08
22	$*B^* \leftrightarrow **C$		0.90	0.84	0.06	1.22	1.16	0.07
23	$A^{**} \leftrightarrow **C$		1.00	0.94	0.07	0.79	0.73	0.07

[a]Reactions 1−8 are adsorption reactions, 9−17 are surface reactions, and 18−23 oxygen transfer reactions. Gibbs reaction free energies (ΔG_r) are given for the adsorption steps together with the corresponding enthalpies (ΔH_r) and entropy contributions ($-T\Delta S_r$). For the surface and oxygen transfer reactions, we report forward ($\Delta E_f^{\ddagger}$) and backward ($\Delta E_b^{\ddagger}$) reaction barriers, the enthalpy barriers ($\Delta H_f^{\ddagger}$, $\Delta H_b^{\ddagger}$), and the entropic contribution ($-T\Delta S_f^{\ddagger}$, $-T\Delta S_b^{\ddagger}$) to the free energy barrier. All energies are reported in electronvolts and given at 650 K and p_{O_2} = 21.4 mbar, p_{CO} = 11.0 mbar, p_{CO_2} = 0 mbar. K are the equilibrium coefficients.

Kinetic Simulations. The kinetic simulations are performed at typical CO oxidation conditions.[22] The temperature dependence of the turnover frequencies are shown in Figure 3 for regular Pt(111), Pt-skin, and SnO_2/Pt(111)/Pt_3Sn. The CO and O_2 partial pressures are set to 21.4 and 11.0 mbar, respectively, and the CO_2 pressure is set to zero. The SnO_2/Pt(111)/Pt_3Sn surface shows clearly an increased activity at lower temperatures as compared to the metal-only surfaces. We find a marked difference in the light-off temperature where the lowest temperature is predicted for SnO_2/Pt(111)/Pt_3Sn and the highest for Pt-skin. The lower light-off temperature for the interface system is related to the facile CO oxidation at the SnO_2/Pt rim which is shown clearly by a decomposition of the total TOF (inset in Figure 3). It is only the Mars−van Krevelen reactions at the interface that contribute to the low temperature activity. The Langmuir−Hinshelwood reactions in the interface system have a kinetic behavior similar to the metal-only surfaces. The apparent activation energy of the reaction on the interface system was calculated to be 0.20 eV in the temperature interval 440−520 K and 0.33 eV in the temperature interval 400−450 K. This apparent activation is close to the experimentally determined value of 0.37 ± 0.04 eV on PtSn nanoparticles supported on porous silica fitted in the temperature interval 525−555 K with partial pressures 133 mbar for CO and 53 mbar for O_2.[22] Using the same conditions and temperature interval, we obtain an apparent activation

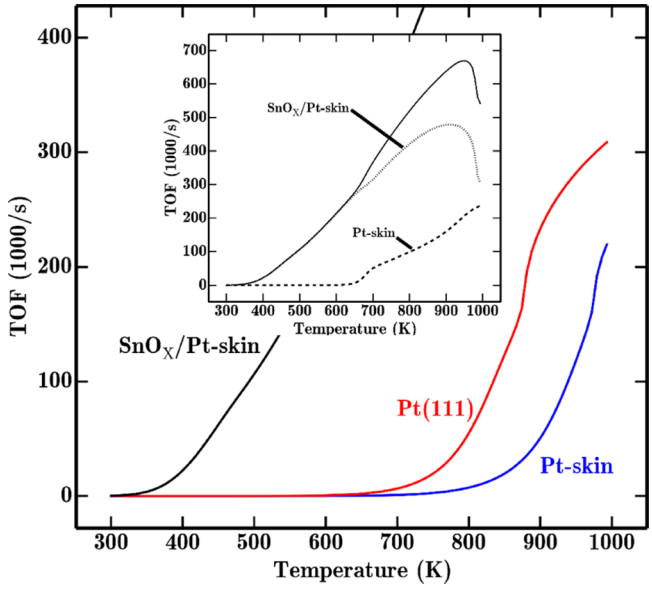

Figure 3. Comparison of the turn over frequency (TOF) for Pt(111), Pt(111)/Pt_3Sn, and SnO_X/Pt(111)/Pt_3Sn. (inset) Different contributions to the total TOF for SnO_X/Pt(111)/Pt_3Sn. The partial pressures for CO and O_2 are 11.0 and 21.4 mbar, respectively.

DOI: 10.1021/acscatal.7b02094
ACS Catal. 2017, 7, 7431−7441

energy of 0.18 eV (525−555 K) with the SnO_X/Pt model; and 0.36 eV in a 100 K earlier temperature interval (419−447 K). A similar value (0.30 eV) has been reported for CO oxidation starting from a $Pt_3Sn(111)$ single crystal with CO and O_2 partial pressures of 0.133 and 1.33 mbar in the temperature interval 294−417 K.[19]

The surface coverages are presented for the SnO_X/Pt(111)/Pt_3Sn system in Figure 4. The total coverage of CO, O, SnO_2

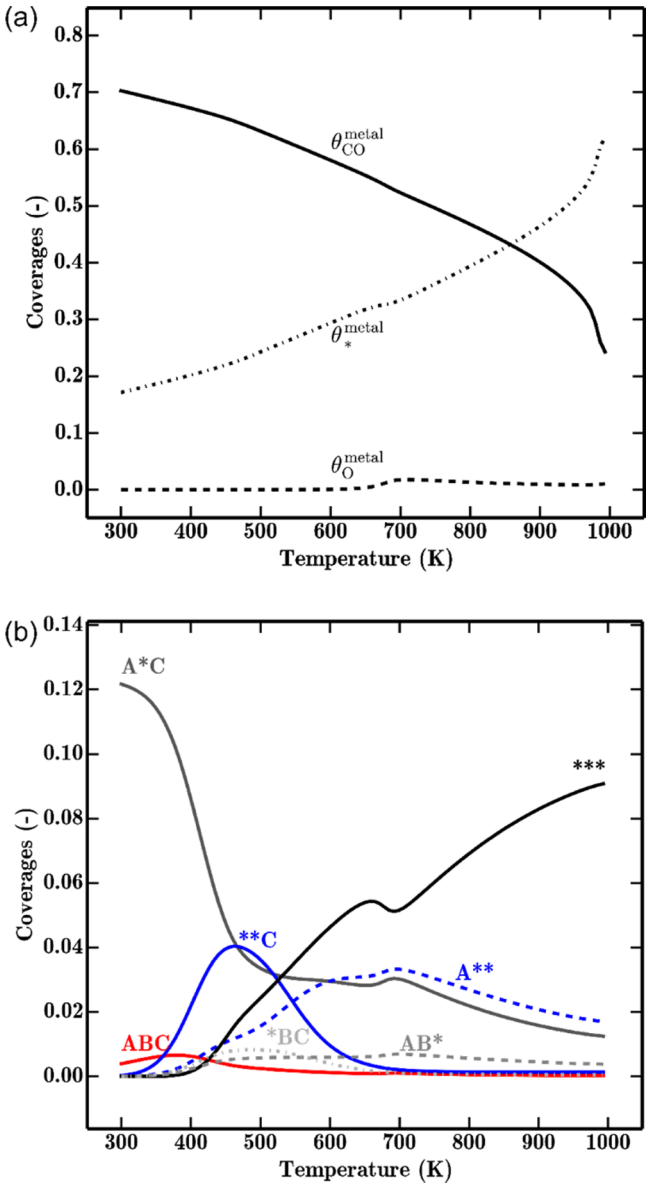

Figure 4. Coverages of the SnO_X states for the SnO_X/Pt(111)/Pt_3Sn model. See Scheme 1 for a description of the states.

and empty sites adds up to unity. The SnO_2 phase blocks 12% of the surface which infers that 88% of the metal sites are available for CO adsorption. The surface is CO poisoned at low temperatures. The metal sites have an oxygen coverage only after light-off (see Figure 4a, around 700 K). This shows clearly that the initial supply of oxygen to the reaction comes from the SnO_2 phase. The different SnO_2 phases are dominated by A*C at low temperature (below 450 K) and by *** at higher temperatures (above 600 K). The initial high abundance of A*C is rationalized by the facile reduction of ABC via CO oxidation. After light-off at the SnO_X/Pt interface, A*C is reduced to **C and A**, and from these states further reduced to ***. The low abundance of states ABC, AB*, and *BC is a consequence of facile reactions (CO oxidation, regeneration) from these states. State *B* is avoided in the reaction network due to high barriers to access this state. Note that the rate of the oxygen regeneration is proportional to the coverage of SnO_X states with at least two vacancies.

Another powerful method to analyze reaction kinetics is the degree of rate control.[49−53] Such an analysis for the SnO_X/Pt(111)/Pt_3Sn systems emphasizes the importance of the SnO_X phase (Figure 5a). The main processes controlling the rate up to 500 K is CO oxidation at the interface. At intermediate temperatures (550−700 K), CO adsorption at the rod and O_2 regeneration of the SnO_X become increasingly important, followed by a regime after light-off (from 750 K) where the oxygen regeneration of SnO_X has the highest influence on the global TOF. From 750 K, the adsorption of CO on the metal-sites has a negative degree of rate control. This can be understood from the competing CO oxidation paths. CO oxidation at the SnO_X/Pt interface requires adsorption of CO whereas an increase of the TOF via Langmuir−Hinshelwood reactions at the metal sites requires CO desorption. In the temperature interval between 750 and 1000 K, regeneration of the SnO_2 phase has a higher rate control than CO adsorption. The rate control analysis shows an increasing importance of O_2 adsorption on the Pt-skin from 650 K (Figure 5a), which corresponds to the light-off of the Langmuir−Hinshelwood path (inset of Figure 3).

A deconvolution of the rate control of the interface oxidation steps is presented in Figure 5b. At low temperature, the rate is controlled by changes between AB* and A** together with A*C to **C which is consistent with the fact that the main contribution to the CO_2 production comes from the interface. At high temperatures, the oxidation from A** to *** gains importance. After the light-off at the metal, the degree of rate control for interface reactions diminishes. The degree of rate control analysis shows that oxygen transfer reactions are of limited importance (Figure 5a). Moreover, the analysis reveals that the ABC, A*C, and **C states of the SnO_X rod are required to properly describe the CO oxidation at the interface. A simplified model could, thus, be anticipated based on these steps only without oxygen transfer reactions. The degree of rate control for the SnO_X/Pt(111)/Pt_3Sn system is markedly different from Pt(111) and Pt(111)/Pt_3Sn where the CO oxidation reaction dominates the rate control.

Experimentally, the CO oxidation reaction over PtSn has been analyzed by determination of the reaction orders.[22] At 473 K and a partial CO pressure of 100 mTorr, the O_2 reaction order was determined to be 0.47 between 40 and 90 mTorr and 0.28 between 90 and 300 mTorr. At these conditions, we calculate the O_2 reaction order to be 0.36 (40−90 mTorr) and 0.21 (90−300 mTorr), respectively. The clear separation in O_2 reaction order between the two pressure regimes is well predicted by the interface model. The reaction order in O_2 was experimentally found to be close to zero for higher CO and O_2 pressures (about 100 Torr for CO and O_2:CO ratio of 1) and temperatures (533 K).[22] At these conditions, our interface model predicts the reaction order in O_2 [between 60 and 100 Torr] to be 0.98. The calculated reaction order for p_{O_2} is, however, very sensitive to the temperature and reduced to 0.29 at 473 K and 0.12 at 423 K. The model is furthermore

DOI: 10.1021/acscatal.7b02094
ACS Catal. 2017, 7, 7431−7441

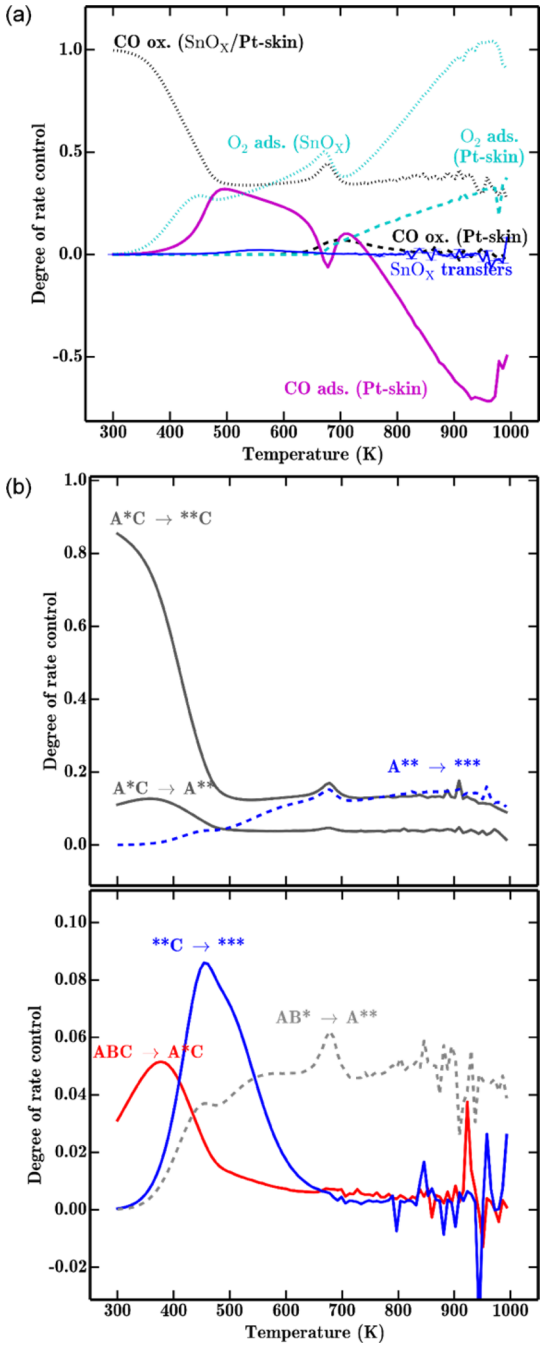

Figure 5. (a) Degree of rate control analysis for the reactions in the $SnO_X/Pt(111)/Pt_3Sn$ model. The different reactions for O_2 adsorption on SnO_X [O_2 ads (SnO_X)], the oxygen transfer reaction within the SnO_X rod [SnO_X transfers], and CO oxidation at the interface [CO ox (SnO_X/Pt-skin)] have been lumped. (b) Degree of rate control for the interface reactions. (upper) Dominant rate controlling reactions. (lower) Reactions with a degree of rate control lower than 0.1.

sensitively dependent on pressure, at O_2 pressures [between 150 and 200 Torr], the reaction order in O_2 is about 0.19 at 473 K and 0.06 at 423 K. We believe that the higher reaction order for our interface model as compared to the experiments is related to the limited number of considered SnO_X surface states and paths for regeneration of the oxygen defects. The decomposition of bulk SnO_2 to SnO is calculated to be endothermic by 2.38 eV, which is an underestimation with respect to the experimental value of 3.08 eV.[54] The discrepancy leads to an underestimation of the exothermicity when reduced SnO_X is regenerated with O_2. These limitations are not crucial at low temperatures, as the oxygen regeneration steps are not rate controlling at these conditions.

Our work demonstrates the importance of *in situ* formed interface effects during CO oxidation on Pt-alloys and alloy nanoparticles, and elucidates further the long-standing debate concerning on the role of Sn in PtSn alloys for CO oxidation reactions. The work is general as it demonstrates that analysis of the surface phase diagram together with microkinetic modeling provides a possibility to understand complex catalytic reactions including reaction induced segregation. Importantly, our microkinetic models accounts for different types of coverage effects.

CONCLUSIONS

Alloy systems are usually employed to tune the activity and selectivity of catalysts. The effects of alloying are generally described in terms of modifications of the electronic properties via ensemble, ligand or strain effects. In the present study we investigated CO oxidation over $Pt_3Sn(111)$. By use of an *ab initio* thermodynamic analysis we demonstrate that Pt_3Sn segregates under realistic oxidation conditions (O_2 and CO partial pressures). The investigated thermodynamically stable phase is SnO_2 and an Sn deficient alloy. The high adsorption energy of CO on Pt is found to promote the segregation, lowering the required O_2 partial pressure for SnO_2 formation. Based on these findings, an interface model was constructed with an SnO_2 rod supported on $Pt(111)/Pt_3Sn$. A mean-field microkinetic model was constructed with 23 reaction steps to explore CO oxidation over this interface system. With the model, we reproduce the low temperature CO activity experimentally observed on PtSn.[11,22] The activity at low temperatures for the $SnO_X/Pt(111)/Pt_3Sn$ system is rationalized by the possibility to have Mars van Krevelen reactions at the interface where CO adsorbed on the metal sites reacts with oxygen from the SnO_2 phase. The reaction path does not suffer from CO poisoning that controls the low temperature reaction rate over Pt(111) or $Pt(111)/Pt_3Sn$ surfaces where the reaction proceeds via a Langmuir−Hinshelwood mechanism. Increasing the temperature, the oxidation reaction lights off at the SnO_X/Pt rim and is rate controlling at low temperatures. At higher temperatures, the metal-only sites will control the rate as such sites are in excess. Previous theoretical studies to elucidate the beneficial effect of alloying Pt with Sn for low temperature CO oxidation have solely focused on electronic alloy effects.[18,19] The present work compares favorably with experiments and provides an alternative mechanism for the low temperature activity over PtSn. Our thermodynamic analysis confirms the recent experimental conclusions that PtSn is segregated during CO oxidation.[12,22] The good agreement between theoretical and experimental apparent activation energies and reaction orders supports the conclusion that the main activity at low temperatures should be attributed to reactions at an SnO_X/Pt interface. While focusing on CO oxidation, this work also has implications for the PROX process, where hydrogen and/or water is expected to aid the regeneration of the SnO_X phase via water, ensuring a fully oxidized or hydroxylated $SnO_X(OH)_Y$ slab.

The present work elucidates the long-standing debate of the role of Sn in PtSn alloys for oxidation reactions and highlights the effects of interfaces formed during operating conditions in heterogeneous catalysis. When combined with microkinetic

DOI: 10.1021/acscatal.7b02094
ACS Catal. 2017, 7, 7431−7441

modeling, we find that interface mechanisms can predict the kinetic behavior reasonably well. This type of model might be important for a range of interface and bimetallic systems where a high CO oxidation activity at low temperature has been reported, for example FeO/Pt[55−59] and Pt/CeO_2,[15,60] and may have implications for catalyst development.

■ ASSOCIATED CONTENT

Supporting Information

The Supporting Information is available free of charge on the ACS Publications website at DOI: 10.1021/acscatal.7b02094.

Atomistic structure files (ZIP)

Additional information on the optimized bulk data, phase diagrams at different temperatures, a detailed account of the kinetic model, and the coverage dependencies of the adsorbates with inclusion of O−CO cross-terms (PDF)

■ AUTHOR INFORMATION

Corresponding Authors

*E-mail: matvan@chalmers.se (M.V.).

*E-mail: ghj@chalmers.se (H.G.).

ORCID

Matthias Vandichel: 0000-0003-1592-0726

Henrik Grönbeck: 0000-0002-8709-2889

Notes

The authors declare no competing financial interest.

■ ACKNOWLEDGMENTS

We thank Mikkel Jørgensen, Maxime Van den Bossche, and Vladimir Zhdanov for fruitful discussions. M.V. acknowledges funding from the Scientific Research-Foundation Flanders (FWO) for a postdoctoral fellowship and a travel grant to visit Chalmers (02/2016-09/2016). Computational resources and services used in this work were provided by VSC (Flemish Supercomputer Center), funded by the Hercules foundation and the Flemish Government−department EWI. The calculations were also performed at C3SE (Göteborg) and PDC (Stockholm) via a SNIC grant. The Competence Centre for Catalysis (KCK) is hosted by Chalmers University of Technology and is financially supported by the Swedish Energy Agency and the member companies: AB Volvo, ECAPS AB, Haldor Topsøe A/S, Scania CV AB, Volvo Car Corporation AB, and Wärtsila Finland Oy.

■ REFERENCES

(1) Rodkin, M.; Tauster, S. J.; Wei, X.; Neubauer, T., In *Innovations in Industrial and Engineering Chemistry*; American Chemical Society, 2008; Vol. *1000*, pp 251−280.

(2) Mizuno, N.; Misono, M. *Chem. Rev.* **1998**, *98*, 199−218.

(3) Farrusseng, D.; Tuel, A. *New J. Chem.* **2016**, *40*, 3933−3949.

(4) Steele, B. C. H.; Heinzel, A. *Nature* **2001**, *414*, 345−352.

(5) Ferrando, R.; Jellinek, J.; Johnston, R. L. *Chem. Rev.* **2008**, *108*, 845−910.

(6) Lam, Y. L.; Criado, J.; Boudart, M. *Nouveau J. Chim.−New J. Chem.* **1977**, *1*, 461−466.

(7) Liu, P.; Norskov, J. K. *Phys. Chem. Chem. Phys.* **2001**, *3*, 3814−3818.

(8) Strasser, P.; Koh, S.; Anniyev, T.; Greeley, J.; More, K.; Yu, C. F.; Liu, Z. C.; Kaya, S.; Nordlund, D.; Ogasawara, H.; Toney, M. F.; Nilsson, A. *Nat. Chem.* **2010**, *2*, 454−460.

(9) Escudero-Escribano, M.; Malacrida, P.; Hansen, M. H.; Vej-Hansen, U. G.; Velazquez-Palenzuela, A.; Tripkovic, V.; Schiotz, J.; Rossmeisl, J.; Stephens, I. E. L.; Chorkendorff, I. *Science* **2016**, *352*, 73−76.

(10) Lindahl, N.; Zamburlini, E.; Feng, L.; Grönbeck, H.; Escudero-Escribano, M.; Stephens, I. E. L.; Chorkendorff, I.; Langhammer, C.; Wickman, B. *Adv. Mater. Interfaces* **2017**, *4*, 1700311.

(11) Moscu, A.; Veyre, L.; Thieuleux, C.; Meunier, F.; Schuurman, Y. *Catal. Today* **2015**, *258*, 241−246.

(12) Moscu, A.; Schuurman, Y.; Veyre, L.; Thieuleux, C.; Meunier, F. *Chem. Commun.* **2014**, *50*, 8590−8592.

(13) Yu, W.; Porosoff, M. D.; Chen, J. G. *Chem. Rev.* **2012**, *112*, 5780−5817.

(14) Liu, K.; Wang, A.; Zhang, T. *ACS Catal.* **2012**, *2*, 1165−1178.

(15) Nguyen, T. S.; Morfin, F.; Aouine, M.; Bosselet, F.; Rousset, J. L.; Piccolo, L. *Catal. Today* **2015**, *253*, 106−114.

(16) Lin, J.; Wang, X.; Zhang, T. *Chinese Journal of Catalysis* **2016**, *37*, 1805−1813.

(17) Fu, Q.; Li, W.-X.; Yao, Y.; Liu, H.; Su, H.-Y.; Ma, D.; Gu, X.-K.; Chen, L.; Wang, Z.; Zhang, H.; Wang, B.; Bao, X. *Science* **2010**, *328*, 1141−1144.

(18) Dupont, C.; Jugnet, Y.; Loffreda, D. *J. Am. Chem. Soc.* **2006**, *128*, 9129−9136.

(19) Dupont, C.; Jugnet, Y.; Delbecq, F.; Loffreda, D. *J. Catal.* **2010**, *273*, 211−220.

(20) Tao, F.; Grass, M. E.; Zhang, Y. W.; Butcher, D. R.; Renzas, J. R.; Liu, Z.; Chung, J. Y.; Mun, B. S.; Salmeron, M.; Somorjai, G. A. *Science* **2008**, *322*, 932−934.

(21) Fernandes, V. R.; Van den Bossche, M.; Knudsen, J.; Farstad, M. H.; Gustafson, J.; Venvik, H. J.; Gronbeck, H.; Borg, A. *ACS Catal.* **2016**, *6*, 4154−4161.

(22) Michalak, W. D.; Krier, J. M.; Alayoglu, S.; Shin, J. Y.; An, K.; Komvopoulos, K.; Liu, Z.; Somorjai, G. A. *J. Catal.* **2014**, *312*, 17−25.

(23) Kim, H. Y.; Henkelman, G. *J. Phys. Chem. Lett.* **2013**, *4*, 216−221.

(24) Radmilovic, V.; Richardson, T. J.; Chen, S. J.; Ross, P. N., Jr *J. Catal.* **2005**, *232*, 199−209.

(25) Schubert, M. M.; Kahlich, M. J.; Feldmeyer, G.; Huttner, M.; Hackenberg, S.; Gasteiger, H. A.; Behm, R. J. *Phys. Chem. Chem. Phys.* **2001**, *3*, 1123−1131.

(26) Jugnet, Y.; Loffreda, D.; Dupont, C.; Delbecq, F.; Ehret, E.; Aires, F.; Mun, B. S.; Akgul, F. A.; Liu, Z. *J. Phys. Chem. Lett.* **2012**, *3*, 3707−3714.

(27) Perdew, J. P.; Burke, K.; Ernzerhof, M. *Phys. Rev. Lett.* **1996**, *77*, 3865−3868.

(28) Kresse, G.; Furthmuller, J. *Comput. Mater. Sci.* **1996**, *6*, 15−50.

(29) Kresse, G.; Furthmuller, J. *Phys. Rev. B: Condens. Matter Mater. Phys.* **1996**, *54*, 11169−11186.

(30) Blochl, P. E. *Phys. Rev. B: Condens. Matter Mater. Phys.* **1994**, *50*, 17953−17979.

(31) Pack, J. D.; Monkhorst, H. J. *Phys. Rev. B* **1977**, *16*, 1748−1749.

(32) Monkhorst, H. J.; Pack, J. D. *Phys. Rev. B* **1976**, *13*, 5188−5192.

(33) Mills, G.; Jonsson, H.; Schenter, G. K. *Surf. Sci.* **1995**, *324*, 305−337.

(34) Henkelman, G.; Jónsson, H. *J. Chem. Phys.* **2000**, *113*, 9978−9985.

(35) Henkelman, G.; Jónsson, H. *J. Chem. Phys.* **1999**, *111*, 7010−7022.

(36) Vandichel, M.; Hajek, J.; Vermoortele, F.; Waroquier, M.; De Vos, D. E.; Van Speybroeck, V. *CrystEngComm* **2015**, *17*, 395−406.

(37) Vandichel, M.; Hajek, J.; Ghysels, A.; De Vos, A.; Waroquier, M.; Van Speybroeck, V. *CrystEngComm* **2016**, *18*, 7056−7069.

(38) Ghysels, A.; Verstraelen, T.; Hemelsoet, K.; Waroquier, M.; Van Speybroeck, V. *J. Chem. Inf. Model.* **2010**, *50*, 1736−1750.

(39) Only orthorombic structures are considered ($\alpha = \beta = \gamma = 90.0$). The optimized cell parameters ($a = b = c$) for the metal(alloy)s Pt, S, Pt_3Sn are 3.97, 6.65, and 4.06/4.82, respectively. For SnO_2 and SnO these are ($a = b$), 4.82 and 3.87 Å in the *a*-direction and 3.24 and 4.91 Å in the *c*-direction, respectively.

(40) Reuter, K.; Scheffler, M. *Phys. Rev. Lett.* **2003**, *90*, 046103.

DOI: 10.1021/acscatal.7b02094
ACS Catal. 2017, 7, 7431−7441

(41) Batyrev, I. G.; Alavi, A.; Finnis, M. W. *Phys. Rev. B: Condens. Matter Mater. Phys.* **2000**, *62*, 4698−4706.
(42) Reuter, K.; Scheffler, M. *Phys. Rev. B: Condens. Matter Mater. Phys.* **2001**, *65*, 035406.
(43) Alavi, A.; Hu, P. J.; Deutsch, T.; Silvestrelli, P. L.; Hutter, J. *Phys. Rev. Lett.* **1998**, *80*, 3650−3653.
(44) Segregation without formation of SnO_2 is energetically less favorable. The reaction of the alloy Pt_3Sn with O_2 to form three Pt units and one SnO_2 unit is favorable with a reaction energy of −3.51 eV. The reaction that converts the alloy Pt_3Sn into two Pt and PtSn has an endothermic reaction energy of 0.36 eV.
(45) Our calculations show that the formation of a bulk oxide structure is thermodynamically prefered. In reality all sorts of SnO_X phases are possible, the better the aggregation of (SnO) and (SnO_2) units on the surface, the more stable the oxide structure formed during reaction conditions. A less stable formed SnO_X structure will result in an upward shift of the segregation line in the phase diagram.
(46) Jones, E. O.T.; Peterson, P. Scipy, open source scinetific tools for Python. http://www.scipy.org/ (accessed Oct 2016).
(47) Vogel, D.; Spiel, C.; Suchorski, Y.; Trinchero, A.; Schlogl, R.; Gronbeck, H.; Rupprechter, G. *Angew. Chem., Int. Ed.* **2012**, *51*, 10041−10044.
(48) Calderon, S. K.; Grabau, M.; Ovari, L.; Kress, B.; Steinruck, H. P.; Papp, C. *J. Chem. Phys.* **2016**, *144*, 044706.
(49) Stegelmann, C.; Andreasen, A.; Campbell, C. T. *J. Am. Chem. Soc.* **2009**, *131*, 8077−8082.
(50) Meskine, H.; Matera, S.; Scheffler, M.; Reuter, K.; Metiu, H. *Surf. Sci.* **2009**, *603*, 1724−1730.
(51) Campbell, C. T. *Top. Catal.* **1994**, *1*, 353−366.
(52) Motagamwala, A. H.; Dumesic, J. A. *Proc. Natl. Acad. Sci. U. S. A.* **2016**, *113*, E2879−E2888.
(53) Campbell, C. T. *ACS Catal.* **2017**, *7*, 2770−2779.
(54) Cox, J. D.; Wagman, D. D.; Medvedev, V. A. *CODATA Key Values for Thermodynamics*; Hemisphere Publishing Corp.: New York, 1989.
(55) Kudernatsch, W.; Peng, G. W.; Zeuthen, H.; Bai, Y. H.; Merte, L. R.; Lammich, L.; Besenbacher, F.; Mavrikakis, M.; Wendt, S. *ACS Nano* **2015**, *9*, 7804−7814.
(56) Freund, H. J. *J. Am. Chem. Soc.* **2016**, *138*, 8985−8996.
(57) Pan, Q. S.; Weng, X. F.; Chen, M. S.; Giordano, L.; Pacchioni, G.; Noguera, C.; Goniakowski, J.; Shaikhutdinov, S.; Freund, H. J. *ChemCatChem* **2015**, *7*, 2620−2627.
(58) Zhao, G.; Yang, F.; Chen, Z.; Liu, Q.; Ji, Y.; Zhang, Y.; Niu, Z.; Mao, J.; Bao, X.; Hu, P.; Li, Y. *Nat. Commun.* **2017**, *8*, 14039.
(59) Chen, H.; Liu, Y.; Yang, F.; Wei, M.; Zhao, X.; Ning, Y.; Liu, Q.; Zhang, Y.; Fu, Q.; Bao, X. *J. Phys. Chem. C* **2017**, *121*, 10398−10405.
(60) Rodriguez, J. A.; Grinter, D. C.; Liu, Z. Y.; Palomino, R. M.; Senanayake, S. D. *Chem. Soc. Rev.* **2017**, *46*, 1824−1841.

DOI: 10.1021/acscatal.7b02094
ACS Catal. 2017, 7, 7431−7441